Progress In Electromagnetics Research, PIER 94, 213–242, 2009

MICROWAVE TOMOGRAPHY EMPLOYING AN ADJOINT NETWORK BASED SENSITIVITY MATRIX

D. G. Drogoudis and G. A. Kyriacou

Microwaves Lab. Kimeria Campus Xanthi
Department of Electrical and Computer Engineering
Democritus University of Thrace
GR-67100, Greece

J. N. Sahalos

Department of Physics
Aristotle University of Thessaloniki
Thessaloniki, GR-54124, Greece

Abstract—A reconstruction algorithm for two- and three-dimensional microwave imaging is proposed. The present effort is focused on the reconstruction of conductivity (σ) and permittivity (ε_r) distributions aiming at a technique serving medical imaging, while permeability imaging can be easily incorporated to serve geophysical geophysical prospecting as well. This work constitutes the most recent one within the effort of extending our Modified Perturbation Method (MPM) from static to high and now microwave frequencies. MPM is an approximate method based on an exact Sensitivity or Jacobian matrix for an iterative update of an initial (σ, ε_r) guess until convergence. This method is proved almost immune of the problem inherent ill-posedness, but its robustness is actually gained by paying a penalty of compromised accuracy in the final achieved image. However, this image can be fine tuned by formulating and solving an exact inverse problem. Regarding the involved Jacobian matrix, this is evaluated through closed form expressions obtained through an Adjoint Network Theorem in conjuction with the electromagnetics reciprocity theorem. The field distributions required for its evaluation are readily available from the always required forward problem solutions on the assumed (σ, ε_r) distributions. Herein, the finite element method along with absorbing boundary conditions are employed for the forward problem electromagnetic simulation.

Corresponding author: G. A. Kyriacou (gkyriac@ee.duth.gr).

1. INTRODUCTION

Microwave tomography is a non-ionizing imaging modality aiming at the reconstruction of a body relative electric permittivity (ε_r) and conductivity (σ) internal distributions and possibly its relative magnetic permeability (μ_r). Geophysical prospecting and medical imaging are among the most attractive applications. The former is justified by the different ($\varepsilon_r, \sigma, \mu_r$) properties of various materials or minerals, [1]. Likewise, biological materials are non-magnetic but they present an inherently high dielectric permittivity and conductivity contrast, [2], enabling their tomographic reconstruction. According to Gabriel, [3], tissue properties are in general ranging from ($\sigma \approx 0.2\,\mathrm{S/m}$, $\varepsilon_r \approx 5$) for bone and fat up to ($\sigma \approx 2.5\,\mathrm{S/m}$, $\varepsilon_r \approx 70$) for tissues with high water content, over the low microwave band. Besides that, the most attractive feature is the tomographicaly exploitable σ- and ε_r-contrast between physiological and malignant tissues as breast [28], ischemic versus normal heart muscle or leukemic marrow versus normal bone, e.g., Fang et al. [4] and the original references therein. Moreover, tissue properties variation with temperature allow their monitoring during hyperthermia treatment, e.g., [5], and the original works cited therein. Besides the efforts in the microwave imaging field, there are a lot of attempts to establish optical imaging modalities, e.g., [22, 26].

Despite the attractive features of microwave tomography and the impressive research effort atracted by it, e.g., [4–9] and [20–30], its evolution has been very slow due to the involved difficulties. The ε_r and σ inhomogeneities causes high scattering which yields a final system matrix dependence on (σ, ε_r), hence it results to a highly nonlinear inverse problem, e.g., [29]. Additionally, the practical restriction in spatial sampling due to limitations in the number of transmitting — receiving antennas along with the non-optimized data collection strategies causes a compromise in the uniqueness of the solution and data independence, e.g., [4, 25]. This can be understood as a highly non-uniform sensitivity distribution (high values close to antennas and very low away from them) which translates to poor system matrix conditioning or equivalently a usually highly ill-conditioned inverse problem. Hence, it is critical to device some optimized data collection strategy and to exploit the available measurements as judiciously as possible in order to reduce the problem ill-conditioning to a manageable level.

Moreover, according to Meaney et al. [10], a lot of attempts to solve the rigorous inverse problem formulated based on Gauss or Gauss-Newton methods required the use of varying degrees of apriori information in order to ensure convergence of the reconstruction

method. Even though, these methods adopted the Levenberg-Marquardt strategy or Tichonov regularization to handle this non-linear inverse problem ill-posedeness, e.g., [31] and [20, 21]. Our present effort tries exactly to contribute toward the direction of providing a very good approximate solution through a robust iterative perturbation technique, almost immune to ill-posedeness. Specifically, the Modified Perturbation Method (MPM) we have initially proposed for static imaging, [11] and extended toward high [12] and microwave [13, 14] frequencies will be fully deployed herein toward both two- and three-dimensional microwave imaging. For the required sensitivities, the exact Jacobian matrix evaluated in closed form based on the Electromagnetics Reciprocity Theorem and Adjoint-Field approach. Since this iterative MPM technique is proved almost immune to the problem of ill-posedenes, by paying the penalty of a compromised accuracy, the resulting (σ, ε_r) after a few iterations (up to 10–15 iterations) can serve as the required very good starting solution for an exactly formulated inverse problem. This constitutes one of our next tasks. Namely, to use the already obtained Jacobian matrix to setup the Hessian matrix and formulate an exact Gauss-Newton approach, e.g. [31]. This will be solved iteratively exploiting the (σ, ε_r) distributions obtained through MPM as initial guesses. Actually, this method will fine-tune the MPM solutions starting from one near the global minimum, avoiding the non-uniqueness or local minima traps. Moreover, an attempt to device a data collection strategy reducing the ill-posedeness (or maximizing the available information) will be tried herein based on a singular value decomposition of the Jacobian matrix. Particular attention will be given to the establishment of a three-dimensional data collection and the associated reconstruction algorithm, since this improves the uniqueness of the solution as also referred in [4, 23, 24, 27–29].

The involved forward problem is solved employing a Finite Element Method, where the unbounded solution is truncated using Absorbing Boundary Conditions (ABC). A dual mesh approach is adopted, e.g., [4], where a fine forward mesh is used for the solution of the forward problem (Maxwell equations), while (σ, ε_r) distributions are discretized and updated on a coarse reconstruction mesh. The spatial resolution of the latter is defined by the number of available linearly independent measurements, which in turn depends on the number of receiving-transmitting antennas.

2. FORWARD PROBLEM FORMULATION AND SOLUTION

The geometrical configuration for the two dimensional scattering problem is shown in Fig. 1(a) and for the three dimensional problem in Fig. 1(b). The body to be imaged is assumed of rectangular shape embedded in a lossy homogeneous surrounding medium. An array of elementary dipoles arranged in multiple rings located on a cylindrical surface enclosing the object (Fig. 1(b)), is used to illuminate the body as well as to measure the scattered field. For the two dimensional case (Fig. 1(a)) a circular array of infinite line sources parallel to z-axis is used, so this type of source yields only an E_z component for the electric field. Absorbing boundary conditions are used for the truncation of the unbounded in principle solution domain.

Aiming at the illumination of the structure from different directions sampling the full azimuth and as wide as possible elevation domain, each one of the evenly spaced dipole antennas is successively activated. Since, elementary dipoles are considered their current density is approximated as uniform $\vec{J}_s = J_0\vec{r}$. In our previous work, [14] the convenient special case of z-oriented dipoles is studied. However, working toward the generalization of the analysis arbitrary oriented dipoles are assumed herein. Hence, starting from Maxwell equations for time harmonic fields:

$$\vec{\nabla} \times \vec{E} = -j\omega\mu\vec{H} \tag{1a}$$

$$\vec{\nabla} \times \vec{H} = j\omega\varepsilon_c\vec{E} + \vec{J}_s \tag{1b}$$

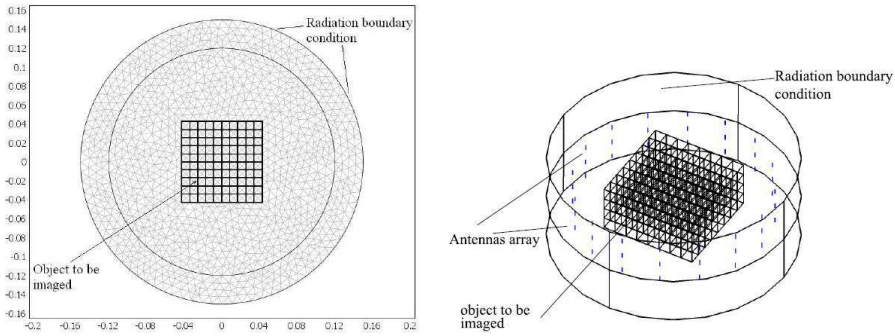

Figure 1. Geometrical configuration of the scattering problem: (a) two-dimensional (2D) and (b) three-dimensional (3D) structure.

where

$$\varepsilon_c = \varepsilon_0\varepsilon_r(1 - j\tan\delta) = \varepsilon\left(1 - j\frac{\sigma}{\omega\varepsilon}\right) = \frac{1}{j\omega}(\sigma + j\omega\varepsilon) \tag{2}$$

The vector Helmholtz equation for the electric field is derived:

$$\vec{\nabla} \times \ \mu_r^{-1}\vec{\nabla} \times \vec{E} - k_0^2\left(\varepsilon_r - j\sigma/\omega\varepsilon_0\right)\vec{E} = -j\omega\mu_0\vec{J}_s \tag{3}$$

where $k_0 = \omega/c$ the free space wavenumber.

For the two dimensional structure illuminated by a $\hat{z}$-oriented infinite line source, the forward scattering problem is governed by the scalar Helmholtz differential Equation (4):

$$\nabla^2 E_z(\vec{r}) + k_0^2\left(\varepsilon_r - j\frac{\sigma}{\omega\varepsilon_0}\right)E_z(\vec{r}) = j\omega\mu_0 J_z(\vec{r}) \tag{4}$$

Following the classical variational formulation procedure the boundary value problems (3), (4) are reduced to the minimization of the following functionals [15]:

$$\begin{aligned} \text{3D:} \quad F(\vec{E}) \ &= \ \frac{1}{2}\iiint_V \left[\frac{1}{\mu_r}\vec{\nabla} \times \vec{E} \cdot \vec{\nabla} \times \vec{E} - k_0^2\varepsilon_c\vec{E}\cdot\vec{E}\right]dV \\ &\quad + \oiint_S \left[\frac{jk_0}{2}(\hat{r}\times\vec{E}) \cdot (\hat{r}\times\vec{E})\right]dS + \iiint_V j\omega\mu_0\hat{J}_z\cdot\vec{E}dV \end{aligned} \tag{5}$$

$$\begin{aligned} \text{2D:} \quad F(E_z) \ &= \ \frac{1}{2}\iint_S \left[\left(\frac{\vartheta E_z}{\vartheta x}\right)^2 + \left(\frac{\vartheta E_z}{\vartheta y}\right)^2 + k_0^2\varepsilon_c E_z^2\right] dS \\ &\quad + \frac{1}{2}\oint_{\Gamma_s}\left(jk_0 + \frac{1}{2r}\right)E_z^2 - \iint_S j\omega\mu_0 J_z E_z dS \end{aligned} \tag{6}$$

The surface integral in Eq. (5) is defined over the fictitious cylinder truncating the solution domain. Likewise the line integral in Eq. (6) is defined along a fictitious circle (Γ_s) terminating the 2-D mesh. Both of these integrals express the absorbing boundary conditions contribution.

A Dual-mesh scheme is employed. The forward field is typically evaluated in a physically larger domain containing not only the target but all of the transmitters, receivers and surrounding structures. For a justification of the necessity of a dual mesh consider the following. Using identical mesh structure for both field and parameter representation will either compromise the forward solver accuracy or will increase the total number of the reconstructed parameters. For most forward modeling methods a minimum mesh density per a given wavelength is typically required (usually smaller than $\lambda/12$) to assure

accuracy of the forward solution. On the other hand, the total element number for the parameter mesh (σ, ε_r) is related to the amount of data available, or the total number of linearly independent measurements. For most microwave imaging cases, the required density of the forward mesh is much higher than that of the parameter mesh.

For the Dual-mesh scheme, the field values are defined on the forward (finer) tetrahedral (triangular for 2D) mesh while the material properties σ and ε_r are defined on the reconstruction (coarser) cubic (rectangular for 2D) mesh. For convenience the two meshes are made conformal. Namely, each cubic element is comprised by a number of tetrahedrals. Hence, each node and edge of the coarse mesh belongs to the finer mesh as well. In this manner field values on the reconstruction mesh are interpolated from the forward mesh and properties values on the forward mesh are interpolated from the reconstruction mesh. For this to be achieved a mapping between the two different meshes needs to be established. Using this scheme a more realistic model and and an accurate forward solution is obtained,while the number of unknowns in the inverse problem is kept lower than the number of available linearly independent measurements.

Since, for the reconstruction mesh the body under consideration is split into cubic (or rectangular) elements with constant σ and ε_r, so a piecewise homogeneous model is constructed as:

$$\varepsilon_c(x,y) = \sum_{k=1}^{E} \varepsilon_{ck}\psi_k, \quad \psi_k = \begin{cases} 1 & \text{within } k\text{-th element} \\ 0 & \text{elsewhere} \end{cases} \tag{7}$$

Using first order tetrahedral vector-edge elements the electric field $\vec{E}$ within each tetrahedral is expanded in terms of the FEM basis functions as, [15]:

$$\text{3D:} \quad \vec{E}^e = \sum_{i=1}^{6} \vec{N}_i^e E_i^e \tag{8}$$

E_i^e denotes the tangential field values along the i-th edge and $\vec{N}_i^e$ is the vector interpolation or basis function given by:

$$\vec{N}_i^e = W_{i_1 i_2} \ell_i^e = \left(L_{i_1}^e \vec{\nabla} L i_2{}^e - L_{i_2}^e \vec{\nabla} L i_1{}^e \right) \ell_i^e \tag{9}$$

The edge numbers and the associated nodes i_1 and i_2 are defined in Table 1 and in Fig. 2(a). For a detailed definition of the quantities involved in (9) one may consult [15, 16].

Likewise for the two-dimensional case first order linear triangular elements are used and the field is expanded in terms of the FEM basis

Table 1. Edge definition for a tetrahedral element.

Edge i	Node i_1	Node i_2
1	1	2
2	1	3
3	1	4
4	2	3
5	4	2
6	3	4

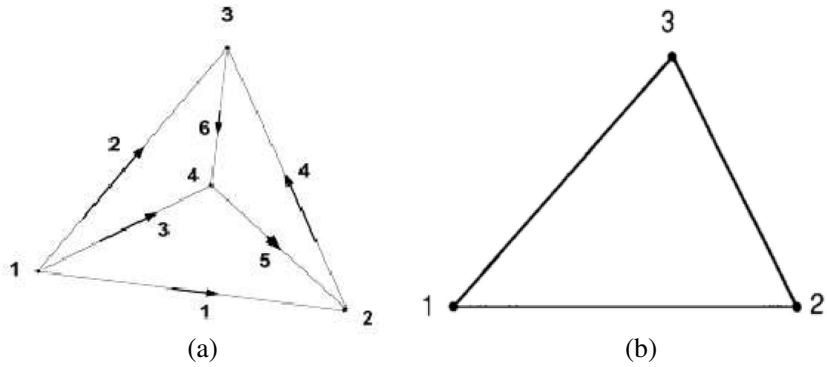

Figure 2. Finite elements employed for the discretization, (a) tetrahedral edge element for 3-D and (b) triangular node element for 2-D.

functions as, [15]:

$$\text{2D:} \quad E_z^e = \sum_{i=1}^{3} N_i^e E_z i^e \tag{10}$$

where $E_z i^e$ denotes the E_z field values on the i-th node and N_i^e is the scalar interpolation or basis function given by:

$$N_i^e = \frac{1}{2\Delta^e}(a_i^e + b_i^e x + c_i^e y), \quad i = 1, 2, 3 \tag{11}$$

Δ^e = area of the e-th element

$a_1^e = x_2^e y_3^e - y_2^e x_3^e$, $b_1^e = y_2^e - y_3^e$, $c_1^e = x_3^e - x_2^e$

a_2^e, a_3^e, b_2^e, b_3^e, c_2^e, c_3^e can be found by cyclic interchange.

A full forward data set requires each antenna to be activated in turn and the scattered electric field to be measured at the location of each receiving antenna. This procedure requires the solution of the scattering problem as many times as the number of the antennas. The ordinary FEM approach is thus employed to yield a linear system of equations as:

$$[K(\epsilon_c)]\,[E] = [B(J_z)] \tag{12}$$

$[K(\epsilon_c)]$ is assembled from the element matrices $[K^e]$ as well as the matrices accounting for the absorbing boundary conditions $[K^s]$, which take the form:

For 3D:

$$[K^e] = \iiint_{V^e} \left[\frac{1}{\mu_r^e} \left\{ \vec{\nabla} \times \vec{N}_i^e \right\} \cdot \left\{ \vec{\nabla} \times \vec{N}_j^e \right\}^T - k_0^2 \varepsilon_c^e \left\{ \vec{N}_i^e \right\} \cdot \left\{ \vec{N}_j^e \right\}^T \right] dV \tag{13}$$

and ABC contribution, [15]

$$[K^s] = \oiint_S \left[\frac{jk_0}{2} (\hat{r} \times \vec{N}_i) \cdot (\hat{r} \times \vec{N}_j) \right] dS \tag{14}$$

For 2D:

$$[K^e] = \iint_{S^e} \left[\frac{\partial N_i^e}{\partial x} \frac{\partial N_j^e}{\partial x} + \frac{\partial N_i^e}{\partial y} \frac{\partial N_j^e}{\partial y} + k_0^2 \varepsilon_c^e N_i^e \cdot N_j^e \right] dS \tag{15}$$

and ABC contribution, [15]

$$[K^s] = \oint_{\partial\Omega} \left(jk_0 + \frac{1}{2r} \right) N_i N_j d\Gamma_s \tag{16}$$

Note that the involved surface integral (14) along the cylindrical (or circular (16)) surface enclosing the solution domain is evaluated by incorporating the appropriate absorbing boundary conditions.

The right hand side of Equation (12) accounts for the impressed current sources defined over the active illuminating antenna as:

$$[B] = \iiint -jJ_z \omega \mu_0 N_j^e \tag{17}$$

In both cases $\hat{r}$ is the unit vector in a direction emanating from a point on the antenna source to boundary element. Using this definition of $\hat{r}$, matrix $[K(\epsilon_c)]$ will vary for each transmitter. This has significant computational consequences as the linear system must be solved independently for each source. To overcome this difficulty an equivalent source point can be assumed common for each transmitting

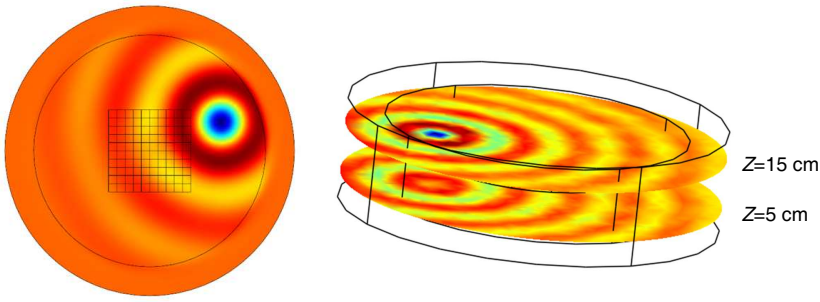

(a) 2D (b) 3D

Figure 3. (a) Electric field distribution when a 2D structure is illuminated by an infinitesimal dipole operated at 800 MHz and (b) electric field distribution at two planes when a 3D structure is illuminated by an infinitesimal dipole operated at 1 GHz.

antenna at the center of the structure according to Fang et al. [4]. This approach provides significant simplification in the enforcement of absorbing boundary conditions along the fictitious surface which terminates the FEM mesh. By this assumption the resulting global matrix $\mathbf{K}$ is independent of the position of the source antenna, so it may be assembled only once for every (σ, ε_r) distribution. For the two-dimensional case, system matrix $\mathbf{K}$ is inverted ($\mathbf{K}^{-1}$) and the field solution for different right hand sides $[B]$ of Equation (12) are readily obtained by a simple multiplication, $[E] = [K]^{-1}[B]$. In three-dimensional the inversion of the matrix $\mathbf{K}$ will consume all the system memory due to the size of the matrix, so an iterative solver is preferred with the appropriate preconditioner. The Generalized Minimum Residual method (GMRES) is used for the solution of the linear system with a symmetric successive over-relaxation-vector (SSOR-vector) preconditioner.

Solving this system the electric fields on the receiving antennas and at all the internal edges or nodes is calculated and stored, to be used later within the reconstruction algorithm. An example of the electric field distribution when one of the infinitesimal dipole or a line-source antenna is activated is shown in Fig. 3.

3. CALCULATION OF THE JACOBIAN MATRIX

The reconstruction algorithm is based on the modified perturbation method that was initially developed for the conductivity imaging in Electrical Impedance Tomography [11] and latter on extended to higher

frequencies (up to 10 MHz) [12]. The aim now is its application in imaging at microwave frequencies. The new algorithm is based again on the Jacobian matrix. The components of the Jacobian are the partial derivatives (or the sensitivities) of the electric field $\vec{E}_r$ measured at the r-th antenna to the complex permittivity ε_c^e of the e-th element-pixel, when the sth antenna is activated. As explained below this is in turn evaluated through closed form expressions resulting from the reciprocity theorem and the employment of an adjoint problem. For this purpose an approach similar to that given by Oldenburg [17] and the original research cited therein is adopted. Namely, the two Maxwell Curl equations are written for the source ($\vec{J}_s$) at s-th antenna and the involved fields ($\vec{E}, \vec{H}$) are differentiated with respect to the e-th complex permittivity. For the adjoint fields ($\vec{E}^\alpha, \vec{H}^\alpha$) these two curl equations are written considering a source ($\vec{J}_r$) at the r-th antenna. The four curl equations are in turn combined following the reciprocity theorem procedure. Specifically, for a dipole antenna at the s-th location the curl equations reads:

$$\vec{\nabla} \times \vec{E} = -j\omega\mu\vec{H} \tag{18a}$$

$$\vec{\nabla} \times \vec{H} = j\omega\varepsilon_c\vec{E} + \vec{J}_s \tag{18b}$$

Taking the derivatives of (18a) and (18b) with respect to ε_{ck} defined in Eq. (7):

$$\vec{\nabla} \times \frac{\vartheta\vec{E}}{\vartheta\varepsilon_{ck}} = -j\omega\mu\frac{\vartheta\vec{H}}{\vartheta\varepsilon_{ck}} \tag{19a}$$

$$\vec{\nabla} \times \frac{\vartheta\vec{H}}{\vartheta\varepsilon_{ck}} = j\omega\varepsilon_c\frac{\vartheta\vec{E}}{\vartheta\varepsilon_{ck}} + j\omega\psi_k(\vec{r})\vec{E} \tag{19b}$$

Consider an auxiliary (adjoint) Maxwell problem with a dipole source $\vec{J}_r$ located at the observation point $\vec{r} = \vec{r}_r$.

$$\vec{\nabla} \times \vec{E}^a = -j\omega\mu\vec{H}^a \tag{20a}$$

$$\vec{\nabla} \times \vec{H}^a = j\omega\varepsilon_c\vec{E}^a + \vec{J}_r \tag{20b}$$

For the application of the Reciprocity theorem procedure to (19a), (19b) and (20a), (20b) according to Balanis [18, p. 324], lets take the inner product of $\vec{H}^a \cdot$ (19a) and $\frac{\vartheta\vec{E}}{\vartheta\varepsilon_{ck}} \cdot$ (20b) and subtract:

$$\begin{aligned} &\vec{H}^a \cdot \vec{\nabla} \times \frac{\vartheta\vec{E}}{\vartheta\varepsilon_{ck}} - \frac{\vartheta\vec{E}}{\vartheta\varepsilon_{ck}} \cdot \vec{\nabla} \times \vec{H}^a \\ = \;& -j\omega\mu\vec{H}^a \cdot \frac{\vartheta\vec{H}}{\vartheta\varepsilon_{ck}} - j\omega\varepsilon_c\frac{\vartheta\vec{E}}{\vartheta\varepsilon_{ck}} \cdot \vec{E}^a - \frac{\vartheta\vec{E}}{\vartheta\varepsilon_{ck}} \cdot \vec{J}_r \end{aligned} \tag{21}$$

Making use of the identity:

$$\vec{\nabla} \cdot (\vec{A} \times \vec{B}) = \vec{B} \cdot (\vec{\nabla} \times \vec{A}) - \vec{A} \cdot (\vec{\nabla} \times \vec{B}) \tag{22}$$

For $\vec{B} = \vec{H}^a$ and $\vec{A} = \frac{\vartheta \vec{E}}{\vartheta \varepsilon_{ck}}$ the left hand side of (21) can be written as $\vec{\nabla} \cdot (\frac{\vartheta \vec{E}}{\vartheta \varepsilon_{ck}} \times \vec{H}^a)$.

In turn, one may take a volume integral of (21) over a domain enclosed by a sphere with a radius tending to infinity and apply the divergence theorem on the left side.

$$\iiint_V (\vec{\nabla} \cdot \vec{F}) du = \oiint_S \vec{F} \cdot d\vec{S} \tag{23}$$

to get:

$$\begin{aligned} &\oiint_S \left(\frac{\vartheta \vec{E}}{\vartheta \varepsilon_{ck}} \times \vec{H}^a \right) \cdot d\vec{S} \\ = &\iiint_V \left(-j\omega\mu \vec{H}^a \cdot \frac{\vartheta \vec{H}}{\vartheta \varepsilon_{ck}} - j\omega\varepsilon_c \frac{\vartheta \vec{E}}{\vartheta \varepsilon_{ck}} \cdot \vec{E}^a - \frac{\vartheta \vec{E}}{\vartheta \varepsilon_{ck}} \cdot \vec{J}_r \right) dV \end{aligned} \tag{24}$$

Likewise, dot-multiplying $\vec{E}^a \cdot$ (19b) and subtracting $-\frac{\vartheta \vec{H}}{\vartheta \varepsilon_{ck}} \cdot$ (20a) yields:

$$\begin{aligned} \vec{\nabla} \left(\frac{\vartheta \vec{H}}{\vartheta \varepsilon_{ck}} \times \vec{E}^a \right) &= \vec{E}^a \cdot \vec{\nabla} \times \frac{\vartheta \vec{H}}{\vartheta \varepsilon_{ck}} - \frac{\vartheta \vec{H}}{\vartheta \varepsilon_{ck}} \cdot \vec{\nabla} \times \vec{E}^a \\ &= j\omega\varepsilon_c \vec{E}^a \cdot \frac{\vartheta \vec{E}}{\vartheta \varepsilon_{ck}} + j\omega\psi_k(\vec{r}) \vec{E}^a \cdot \vec{E} + j\omega\mu \frac{\vartheta \vec{H}}{\vartheta \varepsilon_{ck}} \cdot \vec{H}^a \end{aligned} \tag{25}$$

Adding (25) and (21) the similar terms are canceled, then the use of vector identities $\vec{A} \cdot \vec{B} = \vec{B} \cdot \vec{A}$ and $\vec{A} \times \vec{B} = -\vec{B} \times \vec{A}$ results to:

$$\begin{aligned} \vec{\nabla} \left(\frac{\vartheta \vec{H}}{\vartheta \varepsilon_{ck}} \times \vec{E}^a \right) + \vec{\nabla} \cdot \left(\frac{\vartheta \vec{E}}{\vartheta \varepsilon_{ck}} \times \vec{H}^a \right) &= \vec{\nabla} \cdot \left(\frac{\vartheta \vec{E}}{\vartheta \varepsilon_{ck}} \times \vec{H}^a - \vec{E}^a \times \frac{\vartheta \vec{H}}{\vartheta \varepsilon_{ck}} \right) \\ &= -\frac{\vartheta \vec{E}}{\vartheta \varepsilon_{ck}} \cdot \vec{J}_r + j\omega \vec{\psi}_k(\vec{r}) \vec{E}^a \cdot \vec{E} \end{aligned} \tag{26}$$

Taking the volume integral over a domain enclosed in a sphere of an infinite radius and applying the divergence theorem ends up to:

$$\oiint_S \left(\frac{\vartheta \vec{E}}{\vartheta \varepsilon_{ck}} \times \vec{H}^a - \vec{E}^a \times \frac{\vartheta \vec{H}}{\vartheta \varepsilon_{ck}} \right) d\vec{S}$$

$$= \iiint_V (-\frac{\vartheta \vec{E}}{\vartheta \varepsilon_{ck}} \cdot \vec{J}_r + j\omega \vec{\psi}_k(\vec{r}) \vec{E}^a \cdot \vec{E}) dV \tag{27}$$

The left hand side is identically zero, since both fields intensities tend to zero at infinity by simply considering artificially small unbounded medium losses. Hence, (27) finally gives the so called sensitivity equation as:

$$\iiint_V \frac{\vartheta \vec{E}}{\vartheta \varepsilon_{ck}} \cdot \vec{J}_r dV = \iiint_V j\omega \vec{\psi}_k(\vec{r}) \vec{E}^a \cdot \vec{E} dV \tag{28}$$

The sensitivity Equation (28) can be further simplified to yield a closed form for the Jacobian matrix entries ($\frac{\partial \vec{E}}{\partial \varepsilon_{ck}}$) by first introducing the FEM basis functions and by considering the specific receiving-sensing antennas. Starting from the integrals of (28), these are in general over the whole solution domain. But, actually the left hand side is restricted over the current carrying volume (V_r) of the r-th antenna. In turn, considering the definition (7) for the complex dielectric expansion the right hand side integral of (28) is obviously

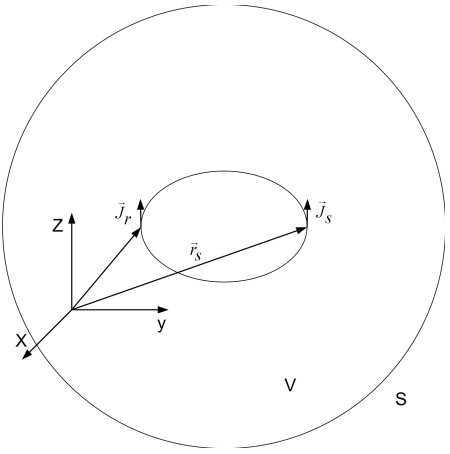

Figure 4. Geometry for the application of the reciprocity theorem.

restricted over the volume (V_k) of the k-th-element. Further a closer look at the dot product of (28) left hand side reveals that the involved electric field is that produced by a radiating antenna at the $\vec{r} = \vec{r}_s$ position (Fig. 4) illuminating the receiving antenna at $\vec{r} = \vec{r}_r$ position (sensing port) with only the field component parallel to its current $\vec{J}_r$ producing a net effect. Hence, the derivative $\frac{\partial \vec{E}}{\partial \varepsilon_{ck}}$ can be identified as the sensitivity of the r-th receiving antenna (r-th sensing port) with respect to the k-th element complex permittivity (ε_{ck}) when the s-th antenna illuminates the structure, or specifically the (s, r, k) entry of the Jacobian matrix, $J_{s,r,k} = \frac{\partial \vec{E}}{\partial \varepsilon_{ck}}$. Since the integration is restricted over the k-th element, then the fields $\vec{E}$ and $\vec{E}^a$ can be expanded into the FEM basis (shape) functions according to (8). In view of the above description (28) can be rewritten in the form:

$$\iiint\limits_{V_r} \frac{\vartheta \vec{E}}{\vartheta \varepsilon_{ck}} \cdot \vec{J}_r dV_r = j\omega \iiint\limits_{V_k} \vec{E}^a \cdot \vec{E} dV_k$$
$$= j\omega \iiint\limits_{V_k} \sum_i E_i^k \cdot N_i^k \sum_j E_i^{ak} \cdot N_j^k dV_k \quad (29)$$

Working toward a closed form expression for the Jacobian matrix, the next step is to consider specific antenna types.

For the two-dimensional (2-D) case when the complex permittivity is assumed homogeneous in the z-direction, along which the structure is assumed infinite, it is convenient to employ infinitely extending thin line sources as illuminating antennas with current density defined by:

$$\text{Line source:} \quad \vec{J}_r = I\delta(\vec{r} - \vec{r}_r)\widehat{z} \quad \text{where } I \text{ is a constant current} \quad (30)$$

In this case the sensitivity entries are readily simplified as:

$$\text{2-D:} \quad J_{((s,r),k)} = \frac{\vartheta \vec{E}(\vec{r})}{\vartheta \varepsilon_{ck}} = \frac{j\omega}{I} \iint\limits_{S_k} \sum_i E_i^k \cdot N_i^k \sum_j E_j^{ak} \cdot N_j^k dS_k \quad (31)$$

for a three dimensional structure (3-D) illuminated by thin elementary dipoles of length ($\Delta\ell$) the current density reads:

$$z\text{-oriented elementary dipole:} \quad \vec{J}_r = I\delta\left(\rho - \rho'\right)\widehat{z} \quad (32)$$

where $\rho = \sqrt{x^2 + y^2}$.

Similarly, the sensitivity equation becomes:

$$\text{3-D:} \quad J_{((s,r),k)} = \frac{\vartheta \vec{E}(\vec{r})}{\vartheta \varepsilon_{ck}} = \frac{j\omega}{I\Delta\ell} \iiint_{V_k} \left(\sum_i E_i^k \cdot N_i^k \right) \cdot \left(\sum_j E_j^{ak} \cdot N_j^k \right) dV_k \quad (33)$$

The above z-oriented current excitations yields a primarily z-polarized electric field which is expected to interact mainly with the ε_{zz} component of a possibly anisotropic complex permittivity. In general, the orientation of the radiating dipoles could be exploited as an additional degree of freedom to extract information from dielectrically anisotropic structures, e.g. [22, 27].

The above sensitivity expressions can be written in matrix form as:

$$J_{((s,r),k)} = \gamma \left[E^k \right] \cdot \left[F^k \right] \cdot \left[E^{ak} \right] \quad (34)$$

where $\gamma = j\omega/I$ or $j\omega/I\Delta\ell$ is the constant term for line source and elementary dipole excitations and

$$\left[F_{ij}^k \right] = \iiint_{V_k} \left\{ N_i^k \right\} \cdot \left\{ N_j^k \right\} dV_k \quad (35)$$

Matrices (vectors) $\left[E^k\right]$, $\left[E^{ak}\right]$ represent the tangential electric fields along the edges of the k-th tetrahedral element in three dimensional case or the E_z electric field on the nodes of the k-th triangular element for the two dimensional case. These fields are already computed during the multiple forward problem solutions performed during the setup of the calculated data-set (once for each illuminating antenna). The matrix $\left[F_{ij}^k\right]$ is a 6×6 matrix in 3D or a 3×3 matrix in 2D and its entries can be constructed from the FEM element matrices, [15].

Recall at this point that FEM is applied on a fine mesh of tetrahedral or triangular elements while the image reconstruction is carried out on a coarse rectangular or cubical mesh. Each reconstruction element consist of a number of forward elements and similarly a number of nodes or edges that belong to these forward elements. Equation (34) results to a partial Jacobian matrix for each triangular or tetrahedral forward element. However, the desired Jacobian is that of the rectangular or cubical reconstruction element. For each evaluation the F^k matrices are assembled together according to a classical FEM procedure to yield a $m \times m$ matrix M^e, where e

the global number of the reconstruction element and m the number of edges or nodes that are inside the e-th element. Note that this matrix depends only on the geometry (independent of ε_{rc}) distribution and its calculated only once. Consequently, the Jacobian matrix of the e-th element reads:

$$J_{((s,r),e)} = \gamma\,[E^e] \cdot [M^e] \cdot [E^{ae}] \tag{36}$$

where $[E^e] = [E_1^e, E_2^e, \ldots, E_m^e]$ and $[E^{ae}] = [E_1^{ae}, E_2^{ae}, \ldots, E_m^{ae}]$.

4. SVD OF THE JACOBIAN MATRIX

The Singular Value Decomposition (SVD) of the total Jacobian matrix representing the whole structure is carried out using Matlab. According to the usual SVD procedure, $\mathbf{J}$ is decomposed into three matrices as:

$$\mathbf{J} = \mathbf{U}\boldsymbol{\Sigma}\mathbf{V}^T \tag{37}$$

where $\mathbf{U} = \{\mathrm{u}_1, \mathrm{u}_2, \ldots, \mathrm{u}_\mathrm{p}\}$ and $\mathbf{V} = \{\mathrm{v}_1, \mathrm{v}_2, \ldots, \mathrm{v}_\mathrm{p}\}$ are both column orthogonal matrices. $\boldsymbol{\Sigma}$ is a diagonal matrix with non-negative real values arranged in decreasing order, i.e., $\boldsymbol{\Sigma} = \mathrm{diag}(\{\sigma\}_{i=1}^p)$ with $\sigma_1 \geq \sigma_2 \geq \ldots \geq \sigma_p \geq 0$. Vectors $\mathrm{u_i}$ and $\mathrm{v_i}$ are referred to as the i-th left and right singular vectors respectively, while σ_i is the i-th singular value. The sequence $\{\sigma_1, \sigma_2, \ldots, \sigma_n\}$ is referred to as the singular spectrum of $\mathbf{J}$.

In this section the impact of operating frequency and the numbers of the antennas used in the singular spectrum of the Jacobian matrix is studied. The analysis will be performed only for the two dimensional case but the conclusions can be generalized to the three-dimensions. The problem configuration used here is defined in Fig. 1(a). The numerical singular spectrum of the Jacobian matrices were computed using different system parameters. In order to compare different spectra the definition for the degree of ill-posedness according to Fang, [4] was used. This definition is a modification of that discussed by Hansen, [19] as:

Definition 1. "*If there exists a positive real number α, for a singular spectrum $\{\sigma_i\}_i^N$, and if $\sigma_i/\sigma_1 = O(\exp(-\alpha i))$, then, α is called the degree of ill-posedness of the spectrum.*"

Hence, according to [19] a linear regression was performed on the series of singular values $\{\log(\sigma_i) - \log(\sigma_1)\}_i^N$ (N is the numerical rank of the Jacobian), where the slope was used to estimate α.

So the singular values spectrum of the Jacobian for various signal frequencies was calculated. The background and the object permittivity and conductivity were first assumed identical $\varepsilon_r = 30$ and $\sigma = 0.3\,\mathrm{S/m}$ (absence of inhomogeneity). The number of the unknown

elements-pixels for the coarse-reconstruction mesh was $K = 100$. Two sets of elementary dipoles arrays were used, one with $N = 16$ dipoles and one with $N = 32$ dipoles. The number of linearly independened measurements for $N = 16$ is $M = N(N-1)/2 = 120$, while for $N = 32$ is $M = 496$. In the first case M is close to the number of reconstruction elements (unknowns) K, so marginal resolution is expected while for $N = 32$ the sensitivity and the ill-posedness is expected to be much better.

In Fig. 5(a) the singular values spectrum for $f = 2.5\,\text{GHz}$ is shown, while Fig. 5(b) represents the corresponding ill-posedness degree (α)

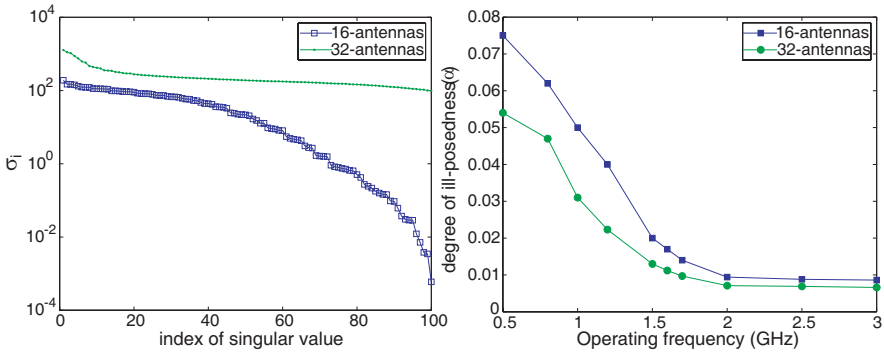

(a) (b)

Figure 5. Jacobian matrix SVD analysis, (a) spectrum of singular values for $f = 2\,\text{GHz}$, (b) degree of ill-posedness as a function of frequency.

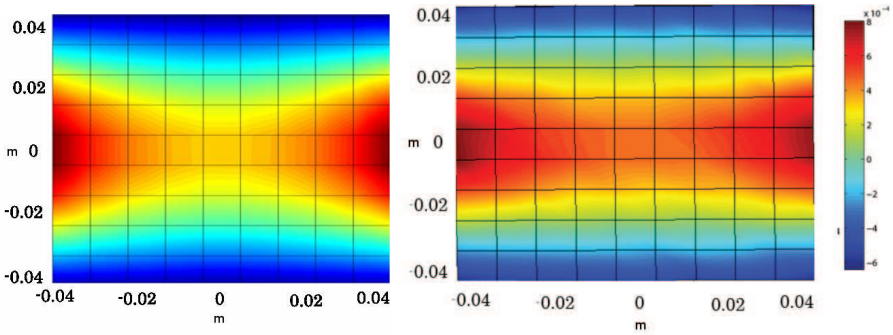

(a) (b)

Figure 6. Plot of a single Jacobian row over the parameter mesh, (a) for $f = 1\,\text{GHz}$, (b) for $f = 2.5\,\text{GHz}$.

versus the operating frequency. From Fig. 5(b) it is observed that for increasing frequencies the degree of ill-posedness is reduced indicating that at these frequencies the reconstructed image quality might be better. Moreover, for $N = 32$ dipoles α is lower than $N = 16$ for all frequencies as expected. One may arrive at a similar conclusion by plotting one row of the Jacobian (one pair of transmitting — receiving antennas) over the reconstruction area for different frequencies, e.g., $f = 1\,\text{GHz}$ and $f = 2.5\,\text{GHz}$. As it is shown in Fig. 6 the sensitivity is higher along the fictitious axes connecting a pair of transmitting and receiving antennas, however its distribution is more uniform for the higher frequency (2.5 GHz).

5. RECONSTRUCTION ALGORITHM

The purpose of this section is the extension of the modified perturbation method (MPM) toward microwave frequencies. The mathematical formulation is identical to that of our previous preliminary work [12] for high frequencies. The actual extension concerns the Jacobian matrix which is studied in the previous section. However, let us describe MPM for high and microwave frequencies in an abstract form, in order for the paper to be self-sustained.

It is convenient to start from the static MPM algorithm and present the procedure to extend it to microwave frequencies. According to our previous work [11] the static MPM reads:

$$\sigma_j^n = \sigma_j^{n-1} + k_1 \frac{\sum\limits_{i=1}^{M} \frac{V_{mi}-V_{ci}}{V_{mi}} \frac{\partial V_i}{\partial \sigma_j}}{\sum\limits_{k=1}^{M} \left| \frac{\partial V_k}{\partial \sigma_j} \right|} \sigma_j^{n-1} \tag{38}$$

where M is the total number of linearly independent measurements, V_{mi} and V_{ci} are the measured and the calculated voltage differences at the i-th port (electrodes pair) and k_1 is the relaxation factor.

Working toward the extension of the algorithm to microwave frequencies the involved voltages will be replaced by complex electric field values, while the sensitivities $\partial V_i/\partial \sigma_j$ will be substituted by the Jacobian matrix entries $\partial \vec{E}/\partial \varepsilon_{ck}$ given in closed form by (36).

Considering the field distribution as an analytical function Cauchy-Riemann conditions apply, which can be written as:

$$\frac{\vartheta E_{real}}{\vartheta \varepsilon_{ck}^{real}} = \frac{\vartheta E_{imag}}{\vartheta \varepsilon_{ck}^{imag}} \quad \text{and} \quad \frac{\vartheta E_{imag}}{\vartheta \varepsilon_{ck}^{real}} = -\frac{\vartheta E_{real}}{\vartheta \varepsilon_{ck}^{imag}} \tag{39}$$

In view of (39) the complex Jacobian matrix calculated from Equation (36) can be decomposed into four sub-matrices by separating

the electric field and the complex permittivity into real and imaginary parts as:

$$J = \frac{\vartheta E}{\vartheta \varepsilon_{ck}} = \frac{\vartheta E_{real}}{\vartheta \varepsilon_{ck}^{real}} + j\frac{\vartheta E_{imag}}{\vartheta \varepsilon_{ck}^{real}} = \frac{\vartheta E_{imag}}{\vartheta \varepsilon_{ck}^{imag}} - j\frac{\vartheta E_{real}}{\vartheta \varepsilon_{ck}^{imag}} \tag{40}$$

The above approach greatly simplifies the reconstruction problem by reducing it to the application of our original MPM [11] once for each sensitivity, similar to our previous quasi-static work [12]. The additional advantage of this approach lies on the separate expressions for conductivity and permittivity imaging.

Specifically using (39) the complex Jacobian matrix **J** can be decomposed into four real submatrices as:

$$J_{ik} = \begin{bmatrix} J_{ik}^{RR} & J_{ik}^{RI} \\ J_{ik}^{IR} & J_{ik}^{II} \end{bmatrix} = \begin{bmatrix} \frac{\partial E_i^{real}}{\partial \varepsilon_{ck}^{real}} & \frac{\partial E_i^{real}}{\partial \varepsilon_{ck}^{imag}} \\ \frac{\partial E_i^{imag}}{\partial \varepsilon_{ck}^{real}} & \frac{\partial E_i^{imag}}{\partial \varepsilon_{ck}^{imag}} \end{bmatrix} \tag{41}$$

In view of the above definition of four real Jacobian submatrices ($J_{ik}^{RR} = J_{ik}^{II}$, $J_{ik}^{IR} = -J_{ik}^{RI}$) Equation (38) can be readily extended to complex permittivity imaging at microwave frequencies by applying (38) once for each real sensitivity (Jacobian submatrix). In each case, the normalized difference of measured (E_{mi}) and calculated (E_{ci}) at a specific sensing antenna (reading $(E_{mi} - E_{ci})/E_{mi}$) is multiplied by the corresponding sensitivity $\partial E_i/\partial \varepsilon_{ck}$. These terms constitute the contribution of the i-th sensing antenna to the correction of the k-th complex permittivity. In turn all contributions are summed and normalized with respect of the total sensitivity $\sum_i \partial E_i/\partial \varepsilon_{ck}$ in order for the sum of the weighting factors (sum of sensitivities) to become unity.

Finally the reconstruction algorithm updating the complex permittivity distribution of the k-th element takes the following form:

$$\varepsilon_{ck}^{n} = \left[\varepsilon_{ck}^{real\,(n-1)} + k_1 W_1 \varepsilon_{ck}^{real\,(n-1)}\right] + j\left[\varepsilon_{ck}^{imag\,(n-1)} + k_2 W_2 \varepsilon_{ck}^{imag\,(n-1)}\right] \tag{42}$$

$$W_1 = \frac{\sum_{i=1}^{M} \dfrac{E_{m\,i}^{real} - E_{c\,i}^{real}}{E_{m\,i}^{real}} \dfrac{\vartheta E_i^{real}}{\vartheta \varepsilon_{ck}^{real}}}{\sum_{k=1}^{M} \left| \dfrac{\vartheta E_k^{real}}{\vartheta \varepsilon_{ck}^{real}} \right|} + \frac{\sum_{i=1}^{M} \dfrac{E_{m\,i}^{imag} - E_{c\,i}^{imag}}{E_{m\,i}^{imag}} \dfrac{\vartheta E_i^{imag}}{\vartheta \varepsilon_{ck}^{real}}}{\sum_{k=1}^{M} \left| \dfrac{\vartheta E_k^{imag}}{\vartheta \varepsilon_{ck}^{real}} \right|} \tag{43}$$

$$W_2 = \frac{\sum_{i=1}^{M} \dfrac{E_{m\,i}^{real} - E_{c\,i}^{real}}{E_{m\,i}^{real}} \dfrac{\vartheta E_i^{real}}{\vartheta \varepsilon_{ck}^{imag}}}{\sum_{k=1}^{M} \left| \dfrac{\vartheta E_k^{real}}{\vartheta \varepsilon_{ck}^{imag}} \right|} + \frac{\sum_{i=1}^{M} \dfrac{E_{m\,i}^{imag} - E_{c\,i}^{imag}}{E_{m\,i}^{imag}} \dfrac{\vartheta E_i^{imag}}{\vartheta \varepsilon_{ck}^{imag}}}{\sum_{k=1}^{M} \left| \dfrac{\vartheta E_k^{imag}}{\vartheta \varepsilon_{ck}^{imag}} \right|} \quad (44)$$

where M is the total number of linear independent measurements, E_{mi} and E_{ci} are the measured and calculated fields at the ith antenna and $k_{1,2}$ are the relaxations factors that may provide faster convergence. The optimum values of k_1, k_2 can be obtained through a numerical investigation. As we see from these equations we use four times the basic equation of the Perturbation method but with different combinations of real and imaginary part of electric fields and Jacobian matrix. Also note that the real and imaginary parts of the reconstructed complex permittivity (42) identifies the relative permittivity and conductivity distributions according to (2).

Observing Equations (40) to (42) or even the original static MPM (38) one may discuss on the expected robustness or the immunity of the method to the problem of ill-posedness. As it is well understood the ill posedness is due to very large variations (of the order of 10^6) of the sensitivity. For example very large sensitivity values ($\partial E_i / \partial \varepsilon_{ck}$) may be observed for the voxels-k around the transmitting antenna and along the axis of transmit — receive antenna pairs. But the sensitivity away from these object regions become very small and may be even lower than the measurement or calculations inaccuracies. When exact inverse problem formulations are employed these large variations in sensitivity yields an ill posed Hessian matrix accompanied by a lot of difficulties during its required inversion. Actually, the very large variation in sensitivity corresponds to very large variation in the Hessian matrix eigenvalues which reflects to a high singularity degree. In contrary, these very low sensitivities occur as very small weighting factors in the summations involved in MPM, e.g. (40) to (42). Thus, the very small sensitivity has negligible contribution in the complex permittivity update, which from a different point of view is shadowed by the higher sensitivities. This is equivalent to discarding very small singular values of the Jacobian (or Hessian), or using relatively large regularization parameter. Hence, the resulting reconstruction algorithm is expected to be robust during the first few iterations and it was indeed proved to converge always in our previous works, e.g. [11–14]. The observed monotonous convergence was independent of the electrodes or antenna locations which greatly affects the sensitivity distribution. This is in turn a clear evidence of the MPM immunity against the problem of ill-posedness. Based on these observations MPM ensures convergence without the sophistication of regularization

techniques. However, the penalty paid by MPM for its robustness is the absence of any control of the implicitly involved regularization. Instead, an exact method may involve a controllable regularization parameter which is gradually reduced from one iteration to the next. The reduction of the regularization parameter allows for the small eigenvalues or low sensitivities to be exploited.

According to Meany et al. [10], most regularization methods require the use of a varying degree of apriori information in order to ensure convergence. In contrary MPM ensures convergence without any apriory information, but its accuracy is compromised by its inability to exploit the hidden low sensitivities. Thus, a logical hypothesis toward accuracy improvement is to formulate an exact inverse problem (e.g., a Gauss-Newton scheme) and exploit the final image provided by MPM as an initial guess (apriori information). The regularization parameter within this scheme can be set to zero or to a very small value, uncovering the very low sensitivities (exploiting the very small eigenvalues) which are expected to fine tune the image within a few iterations. The prove of this hypothesis constitutes one of our next tasks.

6. NUMERICAL RESULTS AND DISCUSSIONS

6.1. Computer Test Approach

The so called "computer test" was employed in all cases throughout this paper. First a "target model" is considered and the forward problem is solved for each illumination position. Namely, the first antenna is activated and the forward problem is solved to calculate and store the electric field at all the remaining — receiving antennas. Each one antenna is activated in turn and the received electric fields are stored to form a complete dataset labeled as "measurements". The reconstruction algorithm starts from a homogeneous model and the desired complex permittivity profile is sought.

6.2. Convergence Criteria

Two convergence criteria are adopted. The more general concerns the "available information", which is determined by the difference between fields "measured" on the target model (E_m) and fields calculated at the n-th iterative solution of the forward problem. As in every minimization approach, the sum of squares (SSQ) is the appropriate figure taking signs in to account. Hence the summation over all

measurements ports (M) gives:

$$\mathrm{SSQ} = \sum_i (E_{meas_i} - E_{calc_i})^2 \tag{45}$$

For comparison purposes it is more convenient to present its normalized value (SSQ_N) with respect to its maximum $(\mathrm{SSQ}_{\max})$ occurring at the first iteration of the inverse problem as:

$$\mathrm{SSQ}_N = \frac{\mathrm{SSQ}}{\mathrm{SSQ}_{\max}} \tag{46}$$

While SSQ is general and can be calculated in all cases, it is only an indirect indication of convergence. Namely, its minimization ensure ε_c convergence when a unique solution is safeguarded. But, this condition may be disturbed by the problem singularity degree, which in turn depends on the data collection strategy. For this purpose the well-posedeness or the singularity degree, of the sensitivity-Jacobian matrix is preliminary examined in Section 4. However a further elaboration is required. Besides this for the particular case of the "computer test" the target or true (σ, ε_r) distributions are available. Hence, the estimated normalized deviations of $(\sigma^n_{calc}, \varepsilon^n_{r_{calc}})$ from their true values at the n-th iteration can be defined as a norm of relative error:

$$\sigma - error = \frac{\sum_i^P \left(\sigma^i_{true} - \sigma^i_{calc}\right)^2}{\sum_i^P \left(\sigma^i_{true} - \bar{\sigma}_{true}\right)^2} \tag{47}$$

$$\varepsilon_r - error = \frac{\sum_i^P \left(\varepsilon^i_{r-true} - \varepsilon^i_{r-calc}\right)^2}{\sum_i^P \left(\varepsilon^i_{r-true} - \bar{\varepsilon}_{r-true}\right)^2} \tag{48}$$

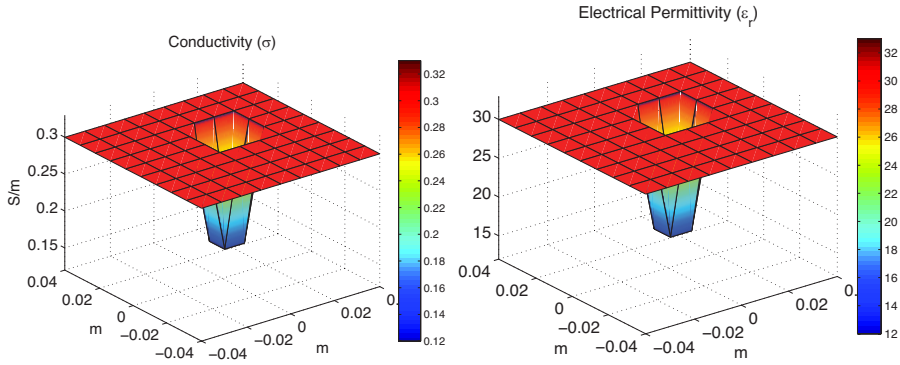

(a) (b)

Figure 7. Target model for the first example (a) conductivity profile, (b) permittivity profile.

where $\bar{\sigma}_{true}$ and $\bar{\varepsilon}_{r-true}$ are the average values of the target profiles and P is the number of elements of the reconstruction mesh.

We should keep in mind that the σ-error, ε_r-error criteria are not applicable for practical in-vivo or even for the "laboratory test" cases where the objects (σ, ε_r) distributions are unknown.

6.3. Two Dimensional Reconstruction

The target model simulated as a computer phantom is presented in Fig. 7. A total number of 32 antennas (line sources) were used, where only 28 are exploited as receivers for each projection angle. A single offset anomaly with conductivity $\sigma = 0.15\,\mathrm{S/m}$ and permittivity $\varepsilon_r = 15$ was introduced in a homogeneous background of $\sigma = 0.3\,\mathrm{S/m}$ and $\varepsilon_r = 30$. The frequency of operation was assumed at $f = 1.1\,\mathrm{GHz}$. The image reconstructed after 9 iterations is presented in Fig. 8 for the conductivity and the permittivity profile respectively. The correct location of the anomaly as well as its σ and ε_r peak values are obtained, but some artifacts are caused.

In a second example with the same configuration, two offset anomalies with conductivity $\sigma = 0.225\,\mathrm{S/m}$ and permittivity $\varepsilon_r = 22.5$ were introduced in a homogeneous background of $\sigma = 0.3\,\mathrm{S/m}$ and $\varepsilon_r = 30$, Fig. 9. The image reconstructed after 9 iterations is presented in Fig. 10 for the conductivity and the permittivity profile respectively.

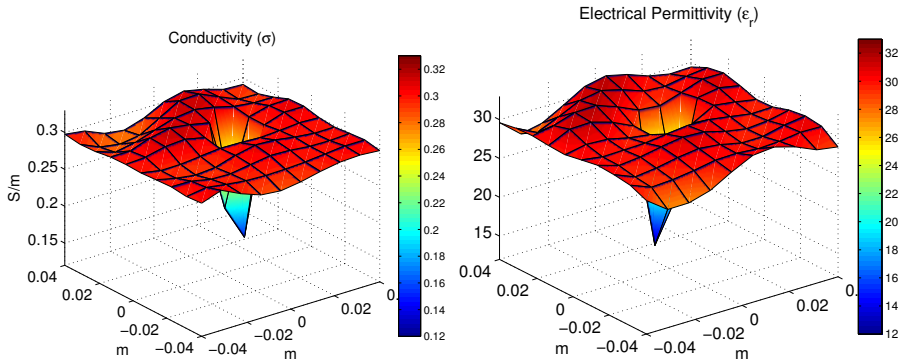

(a) (b)

Figure 8. Reconstructed profiles for the first example of Fig. 7, (a) conductivity and (b) permittivity distributions after 9 iterations. The object is discretized into 100 pixels and is illuminated by 32 line sources at a frequency of 1.1 GHz.

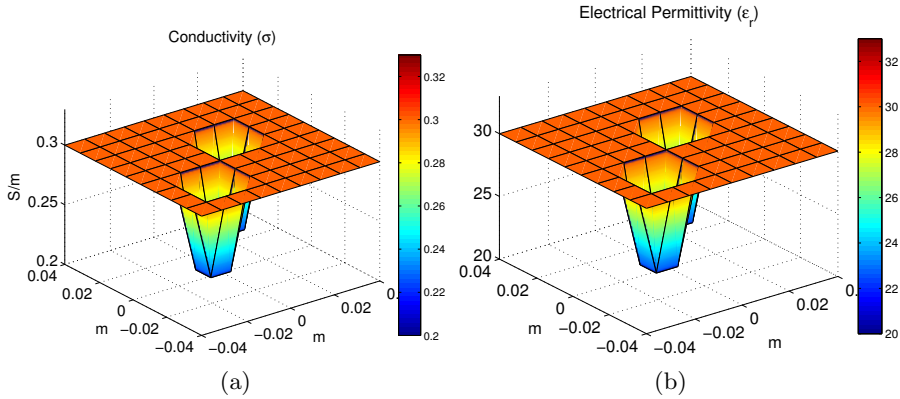

Figure 9. Target model for the second example (a) conductivity profile, (b) permittivity profile.

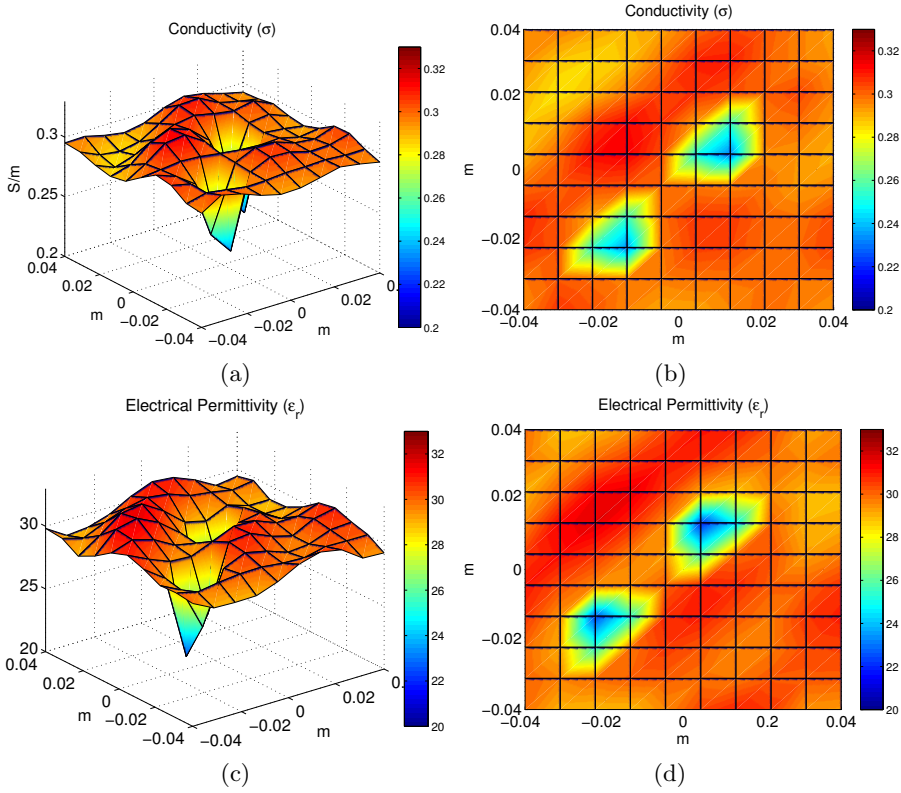

Figure 10. Reconstructed profiles for the second example of Fig. 9 (a) and (b) conductivity, (c) and (d) permittivity distributions after 9 iterations. The object is discretized into 100 pixels and is illuminated by 32 line sources at a frequency of 1.1 GHz.

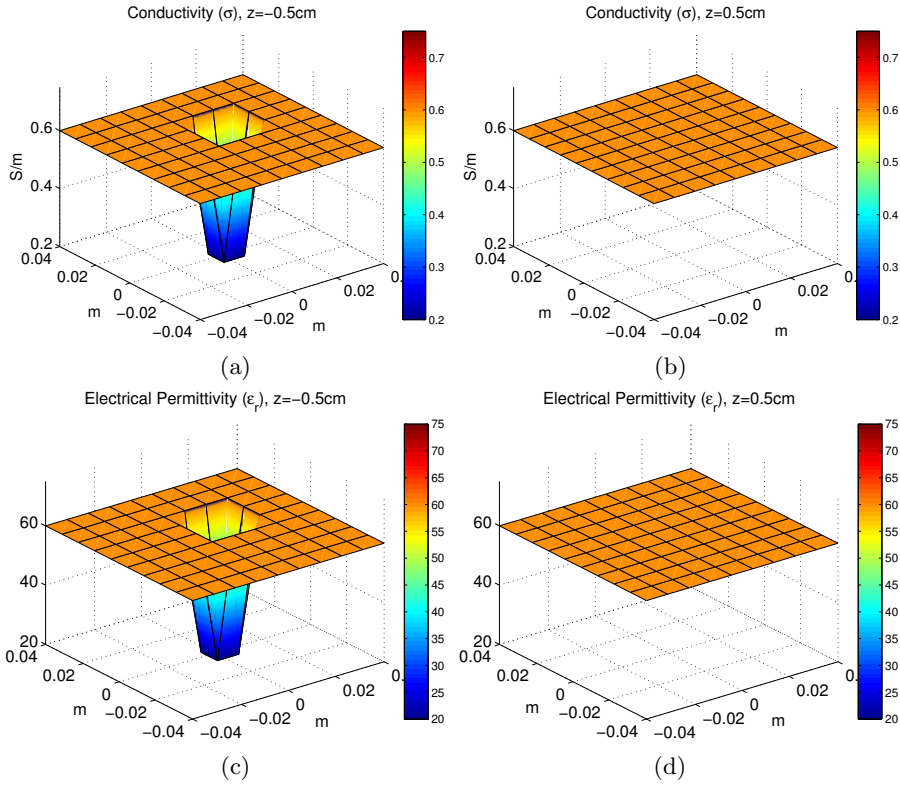

Figure 11. Target model for the third example with profiles (a) 2nd layer conductivity, (b) 1st, 3rd, 4th layer conductivity, (c) 2nd layer permittivity, (d) 1st, 3rd, 4th layer permittivity.

6.4. Three Dimensional Reconstruction

In the third example the reconstruction was made with the 3-D algorithm and the configuration presented in Fig. 1(b) with the object comprised of 4 layers. A total number of 48 antennas arranged in three rings of 16 antennas (elementary dipoles) were used, where only 39 are exploited as receivers for each projection angle. Again a single offset anomaly with conductivity $\sigma = 0.15\,\mathrm{S/m}$ and permittivity $\varepsilon_r = 15$ was introduced at $z = -0.5\,\mathrm{cm}$ (only at the second layer) in a homogeneous background of $\sigma = 0.6\,\mathrm{S/m}$ and $\varepsilon_r = 60$. The frequency of operation was assumed at $f = 1.4\,\mathrm{GHz}$. The target profile is shown in Fig. 11 The image reconstructed after 9 iterations is presented in Fig. 12 for the conductivity and the permittivity profile respectively.

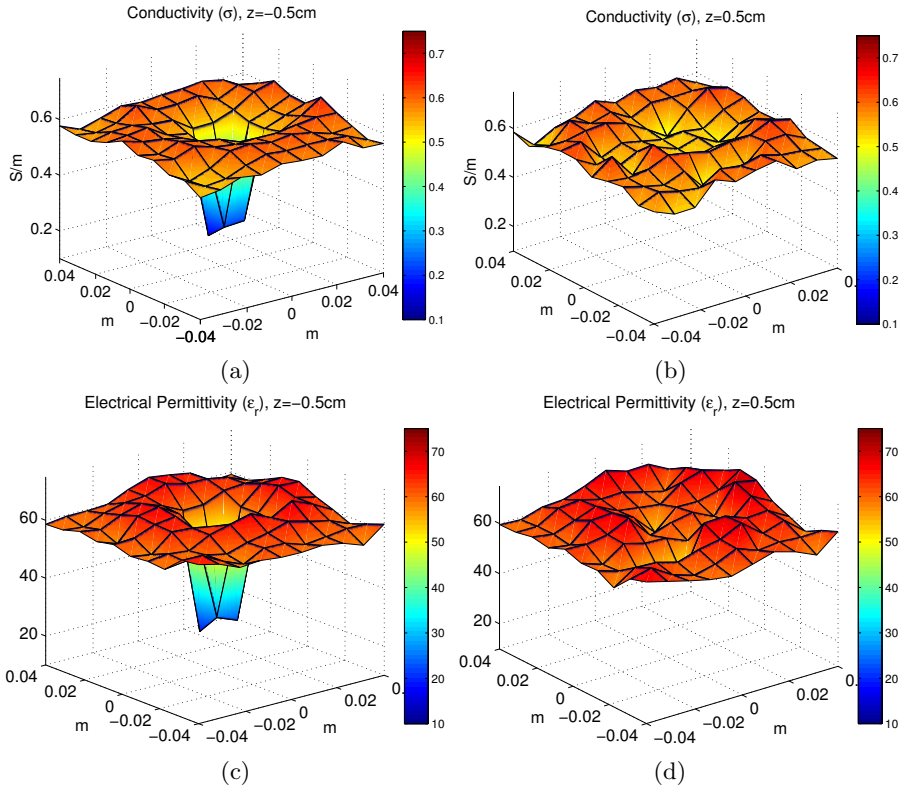

Figure 12. Reconstructed profiles for the third example of Fig. 11 (a) 2nd layer, (b) 3rd layer conductivity, (c) 2nd layer, (d) 3rd layer permittivity distributions, after 9 iterations. The object is discretized into 400 voxels and is illuminated by 48 dipole sources at a frequency of 1.4 GHz.

6.5. Observed Convergence Rate

The normalized mean square errors (46) for the real and imaginary part of electric field distributions are shown in Fig. 13(a) and Fig. 13(b) respectively for the examples given above. As it is observed the convergence rate for each case is similar. The normalized errors between the true and the reconstructed conductivity and permittivity profiles (47), (48) are presented in Fig. 14.

The convergence rate of MPM for the 2-D reconstruction of example −1 is compared against that given in Fang's thesis (Fig. 3.20, p.130), [32] in Fig. 15 and are found similar. Thus MPM seems to have similar performance as compared to the Gauss-Newton method

employed in [32].

A careful observation of Fig. 13 shows that the available information (SSQ) beyond the 6th iteration becomes very small, of the order of 2%. However, there is still some usefull information therein as the expected measurements accuracy is of the order of 0.1%. This reduction of the available information is obviously depicted on the convergence rate of the conductivity and permittivity patterns, since Fig. 14 shows that their convergence rate becomes very small beyond the 6th iteration. Hence, the proposed MPM algorithm performs quite well with a robust behaviour up to 6th iteration. For a further improvement beyond that, especially to improve/reduce the involved

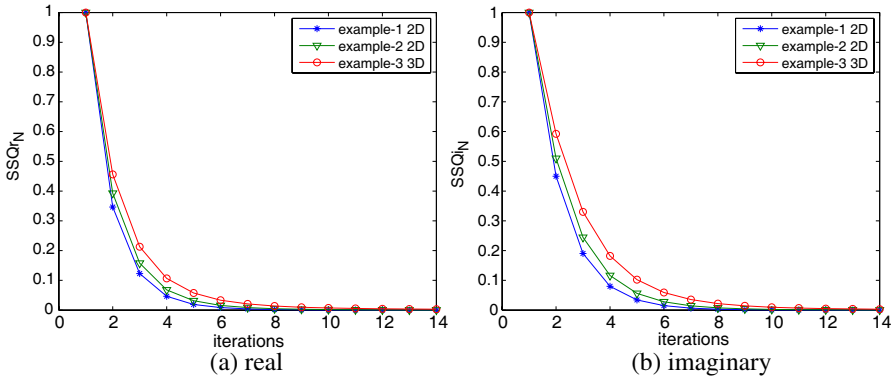

Figure 13. The normalized mean square error of (a) the real part and (b) the imaginary part of the electric field at the sensing antennas.

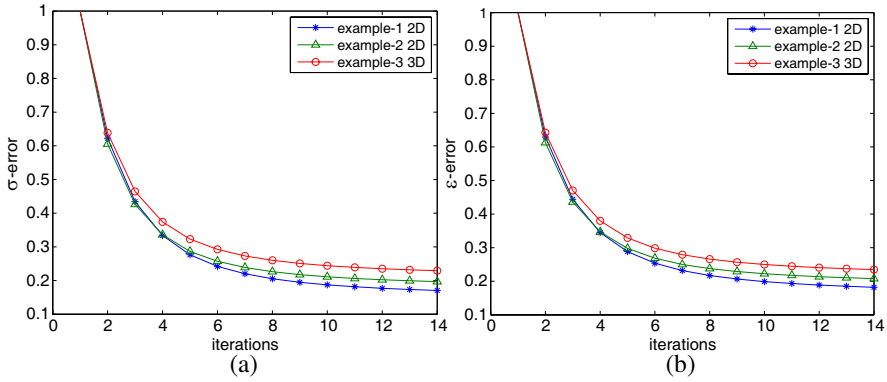

Figure 14. The normalized error between the true and the reconstructed profiles (a) conductivity profile (b) permittivity profile.

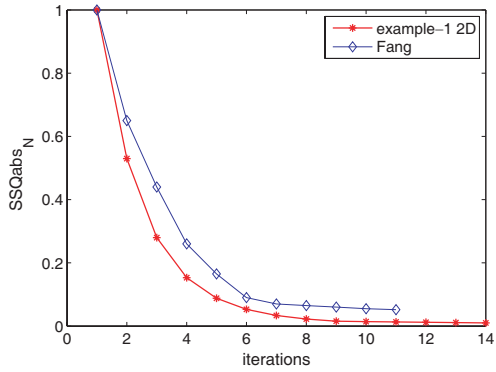

Figure 15. Comparison of the present method convergence rate with that of Fang's thesis, (Fig. 3.20, p. 130), [32].

artifacts, it is necessary to formulate and solve the exact inverse problem e.g., employing an iterative Gauss-Newton approach. The σ- and ε_r-patterns will be used as a very good starting solution very close to the global minimum safeguarding the convergence of the exact inverse algorithm. These observations are in accordance with the reasoning and the tasks layed out in the introduction.

7. CONCLUSION

A modified perturbation method reconstruction algorithm for microwave tomography is successfully established at a computer test level. The key constituent of this algorithm is a close form evaluation of the sensitivity or Jacobian matrix based on an adjoint network and reciprocity theorem approach. The established algorithm is proved robust and able to withstand a large amount of inverse problem ill-posedeness. Despite its simplicity this algorithm is able to successfully localize the target anomalies reaching conductivity and permittivity patterns very close to the expected global minimum at about the 6th iteration. The penalty paid for this simplicity and robustness is a compromise in the finally achieved solution mostly appearing as artefacts around the target anomalies. A further improvement, which also constitutes our next task, refers to the formulation of an exact inverse problem, which may start from the finally obtained image herein and iteratively fine tune it. This can be readily formulated exploiting the exact Jacobian matrix established herein.

ACKNOWLEDGMENT

This work is implemented in the framework of Measure 8.3 through the O.P. Competitiveness 3rd Community Support Programme and is co-funded by: (75%) of the Public Expenditure from the European Union — European Social Fund, (25%) of the Public Expenditure from the Hellenic State — Ministry of Development — General Secretariat for Research and Technology, and Private Sector (INTRACOM SA).

REFERENCES

1. Keller, G. V., "Electrical properties of rocks and minerals," *Handbook of Physical Constemts*, S. P. Calrk (ed.), 553–770, N. Y. Geological Society of America, 1988.
2. Pethig, R., "Dielectric properties of biological materials: Biophysical and medical applications," *IEEE Transactions on Electrical Insulation*, Vol. 19, 453–474, Oct. 1984.
3. Gabriel, C., S. Gabriel, and E. Corthout, "The dielectric properties of biological tissues: Parts 1, 2 and 3," *Phys. Med. Biol.*, Vol. 41, 2231–2249, 1996.
4. Fang, Q., P. M. Meaney, S. D. Geimer, A. V. Streltsov, and K. D. Paulsen, "Microwave image reconstruction from 3-D fields coupled to 2-D parameter estimation," *IEEE Trans. Medical Imaging.*, Vol. 23, No. 4, 475–484, 2004.
5. Meaney, P. M., K. D. Paulsen, A. Hartov, and R. K. Crane, "Microwave imaging for tissue assessment: Initial evaluation in multitarget tissue-equivalent phantoms," *IEEE Trans. Biomed. Eng.*, Vol. 43, 878–890, 1996.
6. Meaney, P., K. Paulsen, and T. Ryan, "Two-dimensional hybrid element image reconstruction for TM illumination," *IEEE Trans. Antennas and Propagation*, Vol. 43, 239–247, Mar. 1995.
7. Semenov, S., R. Svenson, A. Bulyshev, A. Souvorov, A. Nazarov, Y. Sizov, A. Pavlovsky, V. Borisov, B. Voinov, G. Simonova, A. Starostin, V. Posukh, G. Tatsis, and V. Baranov, "Three-dimensional microwave tomography: Experimental prototype of the system and vector born reconstruction method," *IEEE Trans. Biomed. Eng.*, Vol. 46, 937–946, Aug. 1999.
8. Rekanos, I. T., M. S. Efraimidou, and T. D. Tsiboukis, "Microwave imaging: Inversion of scattered near-field measurements," *IEEE Trans. Magnetics*, Vol. 37, 3294–3297, Sep. 2001.
9. Joachimowicz, N., C. Pichot, and J. Hugonin, "Inverse scattering: An iterative numerical method for electromagnetic imaging,"

IEEE Trans. Antennas and Propagation, Vol. 39, 1742–1753, Dec. 1991.

10. Meaney, P. M., K. D. Paulsen, B. W. Pogue, and M. I. Miga, "Microwave image reconstruction utilizing log-magnitude and unwrapped phase to improve high-contrast object recovery," *IEEE Trans. Medical Imaging.*, Vol. 20, No. 2, 104–116, 2001.
11. Kyriacou, G., C. Koukourlis, and J. Sahalos, "A reconstruction algorithm of electrical impedance tomography with optimal configuration of the driven electrodes," *IEEE Trans. Medical Imaging.*, Vol. 12, 430–438, Sep. 1993.
12. Drogoudis, D. G., G. Trichopoulos, G. A. Kyriacou, and J. N. Sahalos, "A modified perturbation method for three-dimensional time harmonic impedance tomography," *PIERS Online*, Vol. 1, No. 2, 151–155, 2005.
13. Drogoudis, D. G., G. A. Kyriacou, and J. N. Sahalos, "A sensitivity matrix based microwave tomography exploiting an adjoint network theorem," *PIERS Online*, Vol. 3, No. 8, 1217–1221, 2007.
14. Drogoudis, D. G., G. A. Kyriacou, and J. N. Sahalos, "A three dimensional microwave tomography employing an adjoint network theorem based sensitivity matrix," *IEEE Trans. Magnetics*, Vol. 45, No. 3, 1686–1689, 2009.
15. Jin, J., *The Finite Element Method in Electromagnetics*, John Wiley & Sons, New York, 1993.
16. Zhu, Y. and A. C. Cangellaris, *Multigrid Finite Element Methods for Electromagnetic Field Modeling*, John Wiley & Sons, 2006.
17. Oldenburg, D. W., "Practical strategies for the solution of large-scale electromagnetic inverse problems," *Radio Science*, Vol. 29, 1081–1099, 1994.
18. Balanis, C. A., *Advanced Engineering Electromagnetics*, John Wiley & Sons, 1989.
19. Hansen, P. C., *Rank-deficient and Discrete Ill-posed Problems: Numerical Aspects of Linear Inversion*, SIAM, Philadelphia, PA, 1997.
20. Semnani, A. and M. Kamyab, "Truncated cosine fourier series expansion methodfor solving 2-D inverse scattering problems," *Progress In Electromagnetics Research*, PIER 81, 73–97, 2008.
21. Semnani, A. and M. Kamyab, "An enhanced method for inverse scattering problems using Fourier series expansion in conjunction with FDTD and PSO," *Progress In Electromagnetics Research*, PIER 76, 45–64, 2007.

22. Shyu, J. J., C.-H. Chan, M.-W. Hsiung, P.-N. Yang, H.-W. Chen, and W.-C. Kuo, "Diagnosis of articular cartilage damage by polarization sensitive optical coherence tomography and the extracted optical properties," *Progress In Electromagnetics Research*, PIER 91, 365–376, 2009.
23. Soleimani, M., C. N. Mitchell, R. Banasiak, R. Wajman, and A. Adler, "Four-dimensional electrical capacitance tomography imaging using experimental data," *Progress In Electromagnetics Research*, PIER 90, 171–186, 2009.
24. Mauriello, P. and D. Patella, "Geoelectrical anomalies imaged by polar and dipolar probability tomography," *Progress In Electromagnetics Research*, PIER 87, 63–88, 2008.
25. Děková, J., "Identification of defects in materials with surface conductivity distribution," *PIERS Online*, Vol. 4, No. 1, 11–15, 2008.
26. Tarvainen, T., M. Vauhkonen, V. Kolehmainen, J. P. Kaipio, and S. R. Arridge, "Utilizing the radiative transfer equation in optical tomography," *PIERS Online*, Vol. 4, No. 6, 655–660, 2008.
27. Mauriello, P. and D. Patella, "Resistivity tensor probability tomography," *Progress In Electromagnetics Research B*, Vol. 8, 129–146, 2008.
28. Zainud-Deen, S. H., W. M. Hassen, E. El deen Ali, and K. H. Awadalla, "Breast cancer detection using a hybrid finite difference frequency domain and particle swarm optimization techniques," *Progress In Electromagnetics Research B*, Vol. 3, 35–46, 2008.
29. Chen, X., D. Liang, and K. Huang, "Microwave imaging 3-D buried objects using parallel genetic algorithm combined with FDTD technique," *Journal of Electromagnetic Waves and Applications*, Vol. 20, No. 13, 1761–1774, 2006.
30. Bermani, E., A. Boni, A. Kerhet, and A. Massa, "Kernels evaluation of svm-based estimators for inverse scattering problems," *Progress In Electromagnetics Research*, PIER 53, 167–188, 2005.
31. Roger, A. and F. Chapel, "Iterative methods for inverse problems," *Progress In Electromagnetics Research*, PIER 5, 423–454, 1991.
32. Fang, Q., "Computational methods for microwave medical imaging," PhD Thesis, Dartmouth College Hanover, New Hampshire, 2004.